

# SpikeDet: Better Firing Patterns for Accurate and Energy-Efficient Object Detection with Spiking Neuron Networks

Yimeng Fan, *Graduate Student Member, IEEE*, Changsong Liu, *Member, IEEE*, Mingyang Li, *Graduate Student Member, IEEE*, Dongze Liu, *Yanyan Liu, Member, IEEE*, and Wei Zhang, *Member, IEEE*<sup>†</sup>

**Abstract**—Spiking Neural Networks (SNNs) are the third generation of neural networks. They have gained widespread attention in object detection due to their low power consumption and biological interpretability. However, existing SNN-based object detection methods suffer from local firing saturation, where neurons in information-concentrated regions fire continuously throughout all time steps. This abnormal neuron firing pattern reduces the feature discrimination capability and detection accuracy, while also increasing the firing rates that prevent SNNs from achieving their potential energy efficiency. To address this problem, we propose SpikeDet, a novel spiking object detector that optimizes firing patterns for accurate and energy-efficient detection. Specifically, we design a spiking backbone network, MDSNet, which effectively adjusts the membrane synaptic input distribution at each layer, achieving better neuron firing patterns during spiking feature extraction. Additionally, to better utilize and preserve these high-quality backbone features, we introduce the Spiking Multi-direction Fusion Module (SMFM), which realizes multi-direction fusion of spiking features, enhancing the multi-scale detection capability of the model. Experimental results demonstrate that SpikeDet achieves superior performance. On the COCO 2017 dataset, it achieves 51.4% AP, outperforming previous SNN-based methods by 2.5% AP while requiring only half the power consumption. On object detection sub-tasks, including the GEN1 event-based dataset and the URPC 2019 underwater dataset, SpikeDet also achieves the best performance. Notably, on GEN1, our method achieves 47.6% AP, outperforming previous SNN-based methods by 7.2% AP with better energy efficiency.

**Index Terms**—Spiking Neuron Network, Object Detection, Neuromorphic Computing.

## I. INTRODUCTION

OBJECT detection is a crucial task in computer vision. It is not only a classification task but also involves regression, requiring the simultaneous identification of object categories and the precise prediction of their locations and sizes [1]. With the development of powerful object detectors [2]–[4], this technology has been applied to wide-ranging fields from autonomous driving [5] to intelligent surveillance [6] and medical imaging [7]. However, high-performance detectors require substantial computational resources, while energy-efficient alternatives sacrifice accuracy, posing challenges for resource-constrained deployments [8], [9].

<sup>†</sup> Corresponding author: Wei Zhang.

Yimeng Fan, Changsong Liu, Mingyang Li, Dongze Liu, and Wei Zhang are with the School of Microelectronics, Tianjin University, Tianjin 300072, China (e-mail: yimengfan@tju.edu.cn; changsong@tju.edu.cn; limingyang97@tju.edu.cn; ldz@tju.edu.cn; tjuzhangwei@tju.edu.cn).

Yanyan Liu is with the Optoelectronic Thin Film Device and Technology Research Institute, Nankai University, Tianjin 300350, China (e-mail: lytianjin@nankai.edu.cn).

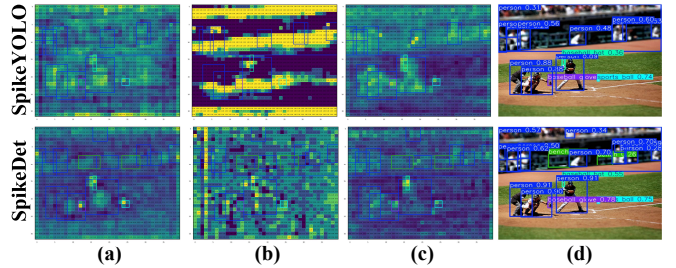


Fig. 1. **Visualization of local firing saturation problem in SNN-based object detector on COCO dataset.** Each pixel represents the neuron firing rate, where yellow indicates higher firing rates and blue indicates lower firing rates. (a) and (b) show feature maps before the detection head, as these features determine both classification and regression. (a) averages the 4D spike tensor ( $[T, C, H, W]$ ) across both time and channel dimensions to show overall spatial firing distribution, while (b) selects a representative channel and averages across time steps to reveal individual neuron firing patterns. (c) shows neuron firing patterns of backbone features at 1/16 resolution. (d) presents the final detection results.

Spiking Neural Networks (SNNs) offer a promising solution to the performance-efficiency trade-off in object detection. Unlike traditional Artificial Neural Networks (ANNs) that rely on continuous values, SNNs communicate between neurons through discrete spiking signals [10]. These spikes, through their temporal dynamic properties, provide SNNs unique information encoding capabilities [11]. Furthermore, this spike-driven mechanism can avoid the computational burden of multiplication operations, instead relying on simpler addition operations. This provides them with significant energy efficiency advantages when deployed on neuromorphic chips, as demonstrated by their implementation on the Speck chip, where power consumption can be as low as 0.7 mW in typical visual processing scenarios [12]. Currently, SNN-based object detection methods have been extensively explored [13]–[21], but their performance remains below that of ANN-based object detectors. Moreover, their energy-efficient advantages gradually diminish as their performance improves [20], [21].

These limitations motivate us to identify a fundamental problem in existing SNN-based detectors. As shown in Fig. 1, we observe that spiking neurons within bounding boxes are highly active. Particularly in central regions of these boxes, where object information is most concentrated [22], [23], spiking neurons consistently reach maximum firing rates (firing saturation). **We define this phenomenon, where multiple adjacent neurons simultaneously exhibit saturated firing patterns, as local firing saturation.** These saturated neurons are detrimental for SNN-based object detection, as in SNNs,

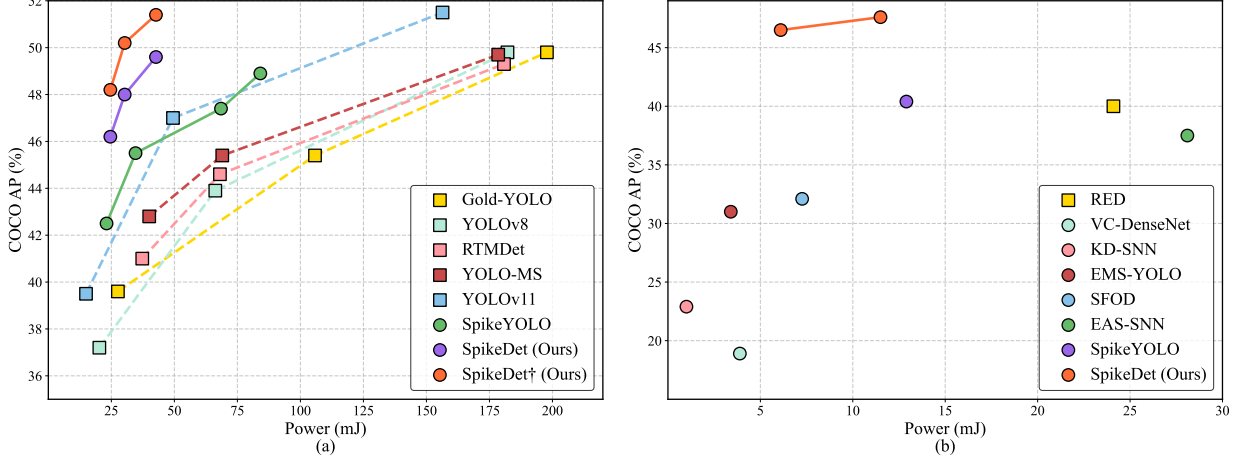


Fig. 2. Comparisons with other state-of-the-art methods on COCO AP and Power consumption. Squares represent ANN-based object detectors, while circles represent SNN-based object detectors. (a) Comparison results on the COCO 2017 dataset. (b) Comparison results on the GEN1 dataset.

features are encoded through neuron firing patterns, which fundamentally differ from ANNs. When multiple neurons in these critical areas reach firing saturation, they produce identical representations, significantly reducing feature discriminability capacity. This issue affects both components of object detection, consequently impacting detection accuracy. Specifically, for classification, reduced feature discriminability causes multiple anchor points to produce similar confidence scores, preventing concentrated object representation and degrading overall confidence. For regression, this generates redundant bounding boxes that waste anchor resources and cause missed detections in overlapping scenes, such as the rear person and bench objects in Fig. 1 (d). Additionally, this local firing saturation issue increases the firing rate of SNN detectors, consequently raising their power consumption.

To address this issue, we propose a novel spiking object detector, SpikeDet, which optimizes the firing patterns of neurons in the model, reducing the probability of local firing saturation to achieve accurate and energy-efficient object detection. The core innovation of our approach is the introduction of a spiking backbone network, **Membrane-based Deformed Shortcut Residual Network** (MDSNet). Current high-accuracy SNN object detectors [15], [20], [21], [24] employ membrane-based shortcuts [25] to achieve residual learning in their backbone networks for enhancing feature extraction capacity. However, this results in the output of the residual path continuously accumulating directly to the shortcut path. Assuming these outputs are approximately independent, membrane synaptic input variance accumulates across successive layers. This variance amplification significantly increases the probability of neurons receiving extremely large input values. This results in increased frequency of neuron firing saturation, consequently causing the aforementioned local firing saturation problem in information-concentrated regions, as shown in Fig. 1(c). For this, we propose the Membrane-based Deformed Shortcut (MDS), which enables the identity mapping to stabilize its output distribution, fundamentally mitigating the local firing saturation problem. Based on MDS and residual architectures,

we design MDSNet, which effectively combines the advantages of both, delivering powerful feature extraction capacity for SNN-based object detectors.

Furthermore, we propose the Spiking Multi-direction Fusion Module (SMFM) to enhance the model's multi-scale representation capability and preserve the neuron firing patterns of backbone features. In traditional spiking fusion methods [17], [20], information flows along limited paths. Consequently, in overlapping multi-scale object scenarios, shallow layers receive large-scale features from deep layers without adequate processing, causing them to fire saturated across entire regions. Multi-direction fusion creates multiple pathways, allowing features to undergo repeated refinement. This reduces excessive synaptic inputs, mitigating local firing saturation while enhancing multi-scale feature utilization.

The main contributions of this work can be summarized as follows:

(1) We propose SpikeDet, an accurate and energy-efficient spiking object detector. The SpikeDet achieves better neuron firing patterns by optimizing the backbone and neck networks, thereby mitigating the local firing saturation problem faced by SNN-based object detectors.

(2) For the backbone, we propose MDSNet, which integrates MDS to regulate the membrane synaptic input distribution of subsequent neurons, enhancing firing pattern stability. For the neck, we design SMFM that implements multi-direction feature fusion in SNNs, preserving stable firing patterns while improving the model's multi-scale detection capability.

(3) Our method achieves better performance. On the COCO 2017 [26], event-based GEN1 [27], and underwater URPC 2019 datasets [28], SpikeDet achieves 51.4%, 47.6%, and 50.1% AP respectively, outperforming other SNN-based approaches while maintaining the lowest power consumption.

The rest of this paper is organized as follows. In Section II, we report the related work. Then we provide the preliminaries of SNNs in Section III. Section IV introduces our proposed method. We present experiment results in Section V. After that, we discuss the hardware deployment of SpikeDet in Section VI. Finally, we conclude this work in Section VII.

## II. RELATED WORK

### A. Spiking Neural Networks

SNNs are designed to mimic biological behavior more accurately than ANNs through spiking neurons [29]. However, the non-differentiable nature of neuron spike firing prevents SNNs from being trained with traditional backpropagation algorithms used in ANNs. To address this challenge, researchers have proposed two training approaches for SNNs: ANN2SNN conversion and direct training. The ANN2SNN conversion approach approximates ReLU activation using average firing rate, allowing trained ANNs to be transformed into SNNs [30]. Although this approach has led to powerful SNNs [13], it requires thousands of time steps. Moreover, this method is suited only for static datasets, and the performance of converted SNNs depends on the original ANNs. Conversely, the direct training method leverages surrogate gradients to optimize SNNs [31], facilitating their training on a variety of datasets and achieving strong performance within a limited number of time steps. This technique enables the widespread application of SNNs in vision tasks [14], [29], [32]. Hence, we employ the direct training strategy in this study.

To advance the performance of SNNs and realize deeper architectures, researchers have proposed numerous SNN-based residual learning methods [25], [33], [34]. Among them, SEW-ResNet [34] and MS-ResNet [25] address gradient issues and train networks exceeding 100 layers. However, the former does not consider the non-spiking convolutions caused by spike addition, while the latter, despite solving this issue, introduces a local firing saturation problem that we identify in this work. This paper further investigates SNN characteristics to enhance feature extraction while maintaining a full-spiking network.

### B. Object Detection

Object detection is an important and highly complex task in computer vision. Early object detection methods relied on hand-crafted features and sliding window approaches, achieving good accuracy in face detection [35]. With the development of Artificial Neural Networks (ANNs), ANN-based methods gradually became mainstream. These can be categorized into two-stage and one-stage object detectors. Two-stage methods consist of a proposal generator and a region-wise prediction subnetwork [36], [37]. Although they can achieve good performance, they have gradually been replaced by one-stage methods due to their complex design and inefficient inference. One-stage methods directly generate object locations and classifications, significantly reducing computational complexity while maintaining competitive accuracy. Representative one-stage detectors include YOLO [38]–[40] and DETR [41], [42] series, which have demonstrated competitive accuracy while maintaining high computational efficiency.

### C. Object Detection with Spiking Neuron Networks

Early attempts to apply SNNs to object detection using ANN2SNN conversion [13], [43] face the challenges of high latency, poor performance, and incompatibility with event cameras. VC-DenseNet [14] and EMS-YOLO [15] pioneer

direct training for SNN-based object detection, achieving promising results on both static and event-based datasets. SFOD [17] first introduces an efficient Spiking Fusion Module for SNNs. SpikeYOLO [20] proposes the I-LIF neuron to address the impact of quantization errors from spiking neurons on object detection, significantly improving the performance of SNN-based detectors. However, both approaches overlook the fundamental differences between SNN-based and ANN-based feature representations, i.e., SNN features are represented through neuron firing patterns, which amplifies their performance gap with ANN-based detectors. Hence, our research enhances the SNN object detector by improving firing patterns.

## III. THE PRELIMINARIES OF SNNs

### A. Spiking Neurons

To achieve a balance between biological plausibility and computation complexity in SNNs, researchers have introduced various spiking neural models, including the Hodgkin-Huxley [44], Izhikevich [45], Leaky Integrate-and-Fire (LIF) [46], and Integer Leaky Integrate-and-Fire (I-LIF) [20] models, among others. In our work, we employ the I-LIF neuron due to its effectiveness in alleviating the quantization error problem in SNNs. The I-LIF neuron model is represented by:

$$\mathbf{u}^{t,n} = \tau \mathbf{h}^{t-1,n} + \mathbf{x}^{t,n-1}, \quad (1)$$

$$\mathbf{o}^{t,n} = \text{Clip}(\text{round}(\mathbf{u}^{t,n}), 0, D), \quad (2)$$

$$\mathbf{h}^{t,n} = \mathbf{u}^{t,n} - V_{th} \cdot \mathbf{o}^{t,n}. \quad (3)$$

Here,  $\mathbf{u}$  represents the membrane potential,  $\mathbf{h}$  the membrane potential retained from the previous time step,  $\mathbf{x}$  the pre-synaptic input, and  $\mathbf{o}$  the output spike. Variables  $t$  and  $n$  denote time step and layer number, respectively. Function  $\text{Clip}(x, \text{min}, \text{max})$  constrains  $x$  within  $[\text{min}, \text{max}]$ , while  $\text{round}(x)$  rounds  $x$  to the nearest integer.  $D$  is the upper limit hyperparameter for integer-valued spike activation,  $\tau$  is the membrane potential decay constant, and  $V_{th}$  is the membrane potential threshold. The core of the I-LIF neuron lies in Eq. 2, which enables neurons to generate integer spikes during training and can convert them to the sum of binary spikes in  $D$  time steps of Soft-Reset IF (SR-IF) neurons during inference. **Proposition 1.** *The integer spikes output by I-LIF neurons during training can be converted to the sum of binary spikes from SR-IF neurons over  $D$  time steps during inference, provided that these SR-IF neurons are configured with: (1) a threshold  $V_{th} = 1$ , and (2) their inputs  $\mathbf{x}^{t,n-1}$  adjusted by a bias of  $0.5(1 - \tau_{I-LIF})^{t-1}$ .*

*Proof.* In SR-IF neurons, the differences from I-LIF neurons lie in their integration and firing mechanisms. Specifically, in the integration process, the decay constant  $\tau_{SR-IF} = 1$ , and their firing mechanism changes to

$$\mathbf{o}^{t,n} = \text{Hea}(\mathbf{u}^{t,n} - V_{th}), \quad (4)$$

where  $\text{Hea}$  represents the Heaviside step function. When converting I-LIF neurons to SR-IF neurons over  $D$  time steps, the inputs must be consistent. We can set the input to the SR-IF neuron at time step  $t = 1$  as the original input, while

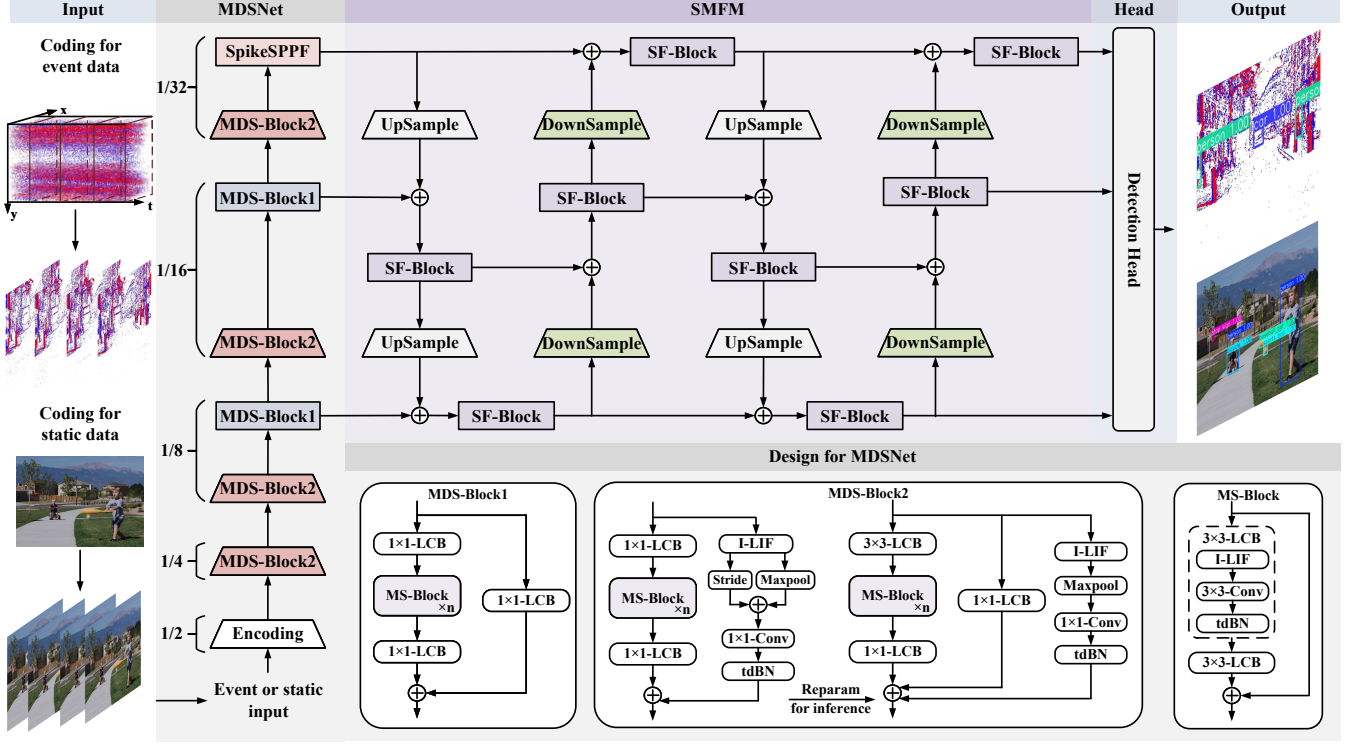


Fig. 3. **The architecture of SpikeDet.** SpikeDet comprises MDSNet, SMFM, and the SpikeYOLO Detection Head [20]. The model receives two types of inputs: event and static data, with the input coding and output represented in the figure. The core of SpikeDet is MDSNet, which consists of 5 stages. Each stage downsampling factor relative to the original input is marked in the figure, with MDS-Block1 and MDS-Block2 performing feature extraction without and with downsampling, respectively. By incorporating MDS, this architecture successfully stabilizes the firing patterns at each stage, alleviating the local firing saturation problem. Additionally, SMFM enables multi-direction feature fusion, allowing features to undergo multiple refinements through the model, thereby improving the model’s capability to detect multi-scale objects and preserving neuron firing patterns.

maintaining zero inputs for time steps  $t = 2, \dots, D$ . Then, with  $V_{th} = 1$ , we can derive,

$$\begin{aligned}
 \mathbf{o}_{I-LIF}^{t,n} &= \sum_{d=1}^D \text{Hea} \left( \mathbf{u}_{SR-IF}^{d,n} - 1 \right) \\
 &= \text{floor}(\text{Clip}(\mathbf{u}_{SR-IF}^{1,n}, 0, D)) \\
 &= \text{Clip}(\text{floor}(\mathbf{u}_{SR-IF}^{1,n}), 0, D) \\
 &= \text{Clip}(\text{round}(\mathbf{u}_{SR-IF}^{1,n} - 0.5), 0, D).
 \end{aligned} \tag{5}$$

To make Eq.5 equivalent to Eq.2, we need to ensure that  $\mathbf{u}_{I-LIF}^{t,n} = \mathbf{u}_{SR-IF}^{1,n} - 0.5$ . To achieve this, we must add appropriate bias to the synaptic inputs of the neuron. According to Eqs.1 and Eq.3, we need to add a bias of  $0.5(1 - \tau_{I-LIF})^{t-1}$  to  $\mathbf{x}^{t,n-1}$ .

Therefore, by performing this conversion during inference, it maintains the spike-driven computation mechanism while reducing quantization errors. Furthermore, to ensure that  $\tau_{I-LIF}$  can function effectively, we employ Soft-Reset LIF neurons at the time steps  $[1, \dots, (t-1) \times D, t \times D, \dots, T \times D]$  when it is deployed. This does not affect the conclusion of Proposition 1, as it only influences how temporal information from the previous time step  $t$  connects to the current one, without impacting the integer spike conversion process.

### B. Power Consumption

The energy efficiency of SNNs primarily comes from performing Accumulation Calculations (ACs) only when neurons fire. However, many current SNN-based works cannot guarantee a full-spiking network. Therefore, when calculating the energy consumption of these networks, we also consider Multiplication and Addition Calculations (MACs). For ANNs, as the vast majority of their operations are MACs with only a small number of ACs, we ignore these ACs operations in our calculations. Furthermore, in line with previous works [15], [17], [19], [21], [47], we quantify the specific power consumption values using  $E_{MACs} = 4.6\text{pJ}$  and  $E_{ACs} = 0.9\text{pJ}$ . The power consumption calculation formulas for SNNs and ANNs are shown respectively as follows, where  $fr$  represents the firing rate of the model,  $T$  denotes the number of time steps, and  $N$  is the number of operations.

$$E_{SNNs} = T \times (fr \times E_{ACs} \times N_{ACs} + E_{MACs} \times N_{MACs}) \tag{6}$$

$$E_{ANNs} = T \times E_{MACs} \times N_{MACs} \tag{7}$$

## IV. METHODOLOGY

### A. Overview

The architecture of our proposed SpikeDet is shown in Fig. 3. As illustrated, the model adopts the backbone-neck-head architecture widely used in object detection frameworks

[4], [8], [17], [38], [40], [42]. For the backbone, we propose MDSNet to extract multi-scale features with more stable firing patterns. For the neck, we design a Spiking Multi-direction Fusion Module (SMFM), which enables the model to enhance backbone features through multi-direction fusion. For the detection head, as it focuses on utilizing already formed features to generate detection results, establishing the stability of the firing pattern is not its critical function. Therefore, we directly adopt the existing SpikeYOLO Detection Head [20].

The spike-driven characteristics of SNNs make them naturally suitable for event data. Consequently, SNN-based detectors are now being explored on not only traditional static datasets but also event-based datasets. To handle both types of data effectively and fully exploit the temporal dynamics of SNNs, we encode the inputs as 4D tensors  $[T, C, H, W]$ , where  $T$  represents time steps,  $C$  denotes the number of channels, while  $H$  and  $W$  correspond to spatial dimensions. For static data, we employ the direct coding method [48], replicating the input  $T$  times to form a time train that supports the temporal processing requirements of the model. For event data, event cameras can asynchronously collect millions of events per second. Each event is defined as  $e_k = (t_k, p_k, x_k, y_k)$ , where  $x_k$  and  $y_k$  are spatial coordinates,  $t_k$  is the timestamp, and  $p_k$  represents polarity. Therefore, to effectively reduce data volume while preserving sparse characteristics, we adopt the coding approach from [20], [25]. This approach first selects a specific time window, divides it into  $T$  temporal bins, and integrates events within each bin into frame format, thereby forming the aforementioned 4D tensor representation. Finally, we use Rate Decoding [17] for model output decoding, followed by Non-Maximum Suppression (NMS) post-processing.

## B. MDSNet

1) *Motivation*: Object detection is a complex task that demands strong feature extraction capabilities from the backbone network. In SNNs, to address this requirement, extensive studies have been conducted on SNN-friendly residual learning approaches [25], [33], [34], as constructing deep networks through residual learning has been proven beneficial in ANNs. Among these efforts, MS-ResNet [25] is the most successful approach, featuring its membrane-based shortcut. Building upon this, subsequent backbones such as EMS-ResNet [15] and S-Backbone [20] have been proposed, enabling the development of advanced SNN-based object detectors. Taking EMS-ResNet as an example, this network can be described as follows,

$$\psi = \text{tdBN} \circ \text{Conv} \circ \text{SN}, \quad (8)$$

$$\mathbf{y}_I^l = \psi(\psi(\mathbf{x}^l)) + \mathbf{x}^l, \quad (9)$$

$$\mathbf{y}_{D1}^l = \psi(\psi(\mathbf{x}^l)) + \text{Cat}[\text{MPool}(\mathbf{x}^l), \psi(\text{MPool}(\mathbf{x}^l))], \quad (10)$$

$$\mathbf{y}_{D2}^l = \psi(\psi(\mathbf{x}^l)) + \psi(\text{MPool}(\mathbf{x}^l)). \quad (11)$$

Here,  $\mathbf{y}$  represents output and  $\mathbf{x}$  represents input. tdBN, Conv, SN, MPool, and Cat denote threshold-dependent Batch Normalization [33], convolution, I-LIF neurons, maxpool, and channel dimension concatenation, respectively. The superscript  $l$  denotes the  $l$ -th residual block, while subscripts  $D$  and  $I$

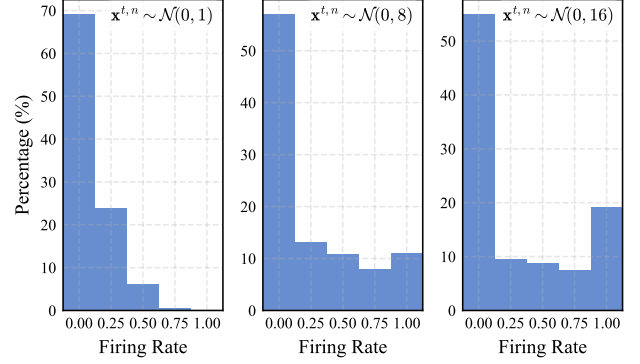


Fig. 4. **Firing rate distribution of I-LIF neurons for different presynaptic input  $\mathbf{x}^{t,n}$  when  $T = 1$  and  $D = 4$ .** Increased variance leads to higher firing saturation probability.

indicate whether the residual block performs downsampling or not. Accordingly, Eq. 9 represents the MS-Block without downsampling, while Eqs. 10 and 11 represent the downsampling blocks EMS-Block1 and EMS-Block2, respectively.

When the model goes deeper, MS-Blocks are stacked repeatedly. For ease, let  $\mathbf{y}_R^l$  denote the residual path output and  $\mathbf{y}_S^l$  denote the shortcut path output. We assume the distributions of these two variables to be  $\mathbf{y}_R^l \sim \mathcal{N}(0, \sigma_R^{l,2})$  and  $\mathbf{y}_S^l \sim \mathcal{N}(0, \sigma_S^{l,2})$ , where  $\sigma_R^{l,2}$  and  $\sigma_S^{l,2}$  represent their respective variances. Assuming the two variables are approximately independent [49],  $\mathbf{y}_I^l \sim \mathcal{N}(0, \sigma_R^{l,2} + \sigma_S^{l,2})$ . Since there is no computation on the shortcut path, for  $k$  stacked MS-Blocks, we can recursively derive that  $\mathbf{y}_I^l \sim \mathcal{N}(0, \sigma_S^{1,2} + \sum_{l=1}^k \sigma_R^{l,2})$ . Therefore, the variance of  $\mathbf{y}_I^l$  becomes increasingly large as the network deepens. This results in unstable membrane synaptic input distribution in subsequent neurons.

**Proposition 2.** *For I-LIF neurons, if the input follows  $\mathbf{x}^{t,n-1} \sim \mathcal{N}(0, \sigma_{in}^{2,2})$ , then the membrane potential follows  $\mathbf{u}^{t,n} \sim \mathcal{N}(0, \sigma_{out}^{2,2})$ , where  $\sigma_{out}^{2,2}$  is proportional to  $\sigma_{in}^{2,2}$ .*

**Proof** The detailed proof is presented in Appendix A.

With Proposition 2, we can conclude that the aforementioned variance accumulation in synaptic input directly creates unstable membrane potential distributions. This instability, according to Eq. 2, increases the probability of neurons firing large integer-valued spikes, thereby exacerbating the local firing saturation problem, severely impacting object detection tasks as discussed in Section I. Fig. 4 confirms our analysis, visually demonstrating that unstable input leads to more active neuron firing patterns. Additionally, as shown in Eqs. 10 and 11, during downsampling, the model positions Maxpool operations before I-LIF neurons. Since Maxpool selects maximum values from local regions, this increases the input intensity received by I-LIF neurons, raising the risk of firing saturation.

2) *MDSNet Architecture*: To address these issues, as shown in Fig. 3, we propose MDSNet, a novel SNN-based ResNet-like backbone network. On the shortcut path, we propose a Membrane-based Deformed Shortcut (MDS), which incorporates I-LIF-1×1Conv-tdBN (1×1-LCB). This structure converts input to spikes through the I-LIF layer and processes them through a 1×1 convolution, which improves expressive-

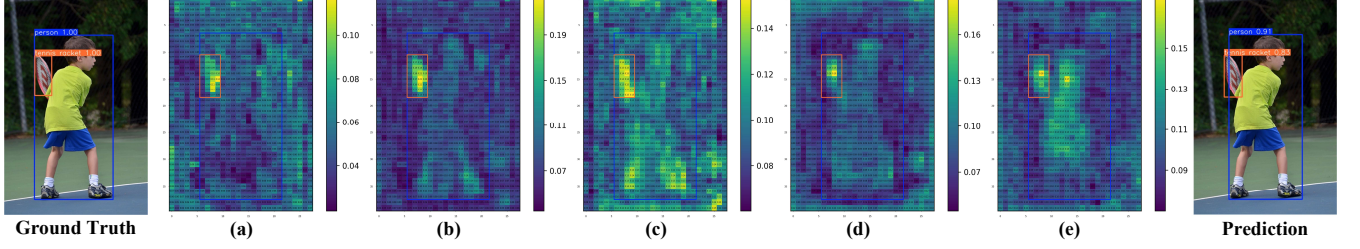


Fig. 5. **Influence of multi-direction feature fusion on firing patterns of SNN-Based detector.** We visualize feature maps at the 1/16 downsampling stage, averaging across  $T$  and  $C$  dimensions to reveal overall firing patterns. Figures (a) to (e) show neuron firing patterns for feature maps with no fusion, one-way, two-way, three-way, and four-way fusion, respectively.

ness capability while allowing batchnorm-scale-fusion with tDBN during inference [33]. Finally, the tDBN component provides this path with the ability to adjust the output distribution. On the residual path, we place MS-Blocks in it rather than on the main path. It provides a clean gradient propagation path for deep networks. Additionally, to avoid the aforementioned problems with stacked MS-Blocks, we place  $1 \times 1$ -LCBs at both the input and output to control variance. Through improvements on both paths, we not only ensure the output distribution stability of each block in MDSNet but also preserve the advantage of efficient information propagation in deep networks offered by the membrane-based shortcut through structure enhancements.

Specifically, MDSNet consists of MDS-Block1 and MDS-Block2. MDS-Block1 is designed without downsampling, following the structure described above. MDS-Block2 serves as the downsampling block. Its residual path is identical to MDS-Block1, but in the shortcut path, we position Maxpool after the I-LIF layer to prevent excessive I-LIF input. Additionally, to better preserve balanced information during downsampling, we also employ fixed stride downsampling. After downsampling, the results from stride downsampling and Maxpool are weighted and added before convolution, followed by tDBN for distribution adjustment. To eliminate non-spiking computations caused by pre-convolution addition during inference, we reparameterize this structure by splitting the shortcut path. One path combines fixed stride downsampling with  $1 \times 1$  convolution to form a  $1 \times 1$ -LCB path, while the other integrates Maxpool after I-LIF of  $1 \times 1$ -LCB.

### C. Analysis of Gradient Vanishing/Explosion for MDSNet

To demonstrate that the MDS does not affect the training and convergence, we use the Block Dynamical Isometry [50] to verify that MDSNet can effectively overcome the gradient vanishing or explosion problem.

Consider a serial network as shown in Eq. 12, where  $f_j$  represents the  $j$ -th layer of the network. The Jacobian matrix from input to output of the  $j$ -th layer can be denoted as  $J_j = \frac{\partial f_j}{\partial f_{j-1}}$ . Furthermore, let  $\phi(J)$  be defined as the expectation of  $\text{tr}(J)$ , while  $\varphi(J) = \phi(J^2) - \phi^2(J)$

$$f(x) = f_L \circ f_{L-1} \circ \dots \circ f_1(x) \quad (12)$$

**Definition 1. (Definition 3.1. in [50])** Consider a neural network that can be represented as a series of blocks as Eq.

12 and the  $j$ -th block's Jacobian matrix is denoted as  $J_j$ . If  $\forall j$ ,  $\phi(J_j J_j^T) \approx 1$  and  $\varphi(J_j J_j^T) \approx 0$ , the network achieves Block Dynamical Isometry and can avoid gradient vanishing or explosion.

**Definition 2. (Definition 5.1. in [50])** Let  $f(x)$  be a transform whose Jacobian matrix is  $J$ .  $f$  is called general linear transform when it satisfies:

$$\phi \left[ \frac{\|f(x)\|_2^2}{\text{len}(f(x))} \right] = \phi(J J^T) E \left[ \frac{\|x\|_2^2}{\text{len}(x)} \right]. \quad (13)$$

**Theorem 1. (Theorem 4.1. in [50])** Given  $J := \prod_{j=L}^1 J_j$ , where  $\{J_j \in \mathbb{R}^{m_j \times m_{j-1}}\}$  is a series of independent random matrices. If  $(\prod_{j=L}^1 J_j)(\prod_{j=L}^1 J_j)^T$  is at least the 1<sup>st</sup> moment unitarily invariant, we have

$$\phi \left( \left( \prod_{j=L}^1 J_j \right) \left( \prod_{j=L}^1 J_j \right)^T \right) = \prod_{j=L}^1 \phi(J_j J_j^T). \quad (14)$$

Since the information transmitted in the network can be considered as random variables [51],  $E \left[ \frac{\|x\|_2^2}{\text{len}(x)} \right]$  is regarded as the second-order moment of the input, denoted by  $\alpha_2$ . Building on the derivations in [15], [33], [50] and Definitions 1 and 2, we can independently analyze each MDS-Block. Subsequently, by applying Theorem 1 to these individual analyses, we can derive the overall behavior of the MDSNet.

**Proposition 3.** For MDSNet, when the encoding layer output follows  $x^t \sim \mathcal{N}(0, 1)$  and each block output follows  $x^{t,j} \sim \mathcal{N}(0, 1)$ , the network satisfies:  $\phi(J J^T) \approx 1$ .

**Proof.** The details can be found in Appendix A.

As elucidated in [15], [25], in the majority of cases,  $\phi(J J^T) \approx 1$  is sufficient to guarantee that the network avoids gradient vanishing or explosion. The condition  $\varphi(J_j J_j^T) \approx 0$  is imposed to preclude the occurrence of accidental situations. Therefore, Proposition 3 provides theoretical support for the ability of MDSNet to address the problem of gradient vanishing or explosion.

### D. SMFM

Research in feature fusion for SNNs is limited to one-way and two-way fusion [17], [20], where large-scale features and small-scale features are combined only a limited number of times. This restricts the transmission of information within the model. For SNNs, this insufficient fusion leads to local firing saturation problems in the center of target regions and creates

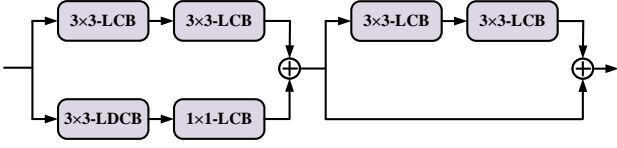


Fig. 6. **The architecture of proposed SF-Block.** The difference between  $3 \times 3$ -LDCB and  $3 \times 3$ -LCB lies in that the former replaces the  $3 \times 3$  convolution with a  $3 \times 3$  depthwise convolution.

excessively high firing responses in irrelevant areas. To address these issues, we propose the Spiking Multi-direction Fusion Module (SMFM). As shown in Fig. 5, after one-way and two-way fusion, compared to the original feature map, the firing responses in irrelevant areas significantly increase, such as in the person’s legs. Moreover, after two-way fusion, the center region of the tennis racket exhibits local firing saturation. These issues are partially mitigated after three-way fusion and are successfully resolved with four-way fusion, which effectively combines multi-scale information while preserving firing patterns.

The structure of the SMFM is shown in Fig. 3. In this module, feature maps ranging from  $1/8$  to  $1/32$  are fused. During the fusion process, we first fuse feature maps of lower resolution with those of higher resolution through upsampling. Following this, we employ downsampling to further integrate these fused feature maps. This process is then repeated iteratively. Next, we will discuss the methods for upsampling, downsampling, and spiking feature fusion.

To achieve upsampling/downsampling, we use Nearest-Neighbor Interpolation (NNI) and  $3 \times 3$  convolution with stride 2 as core elements, and combine these components with LCB. For feature fusion, we multiply the feature maps by learnable constants and then add them together. These constants can be fused with the previous tDBN layer, and since the features are presynaptic inputs that are directly fed into neurons, this method is SNN-friendly. In this way, we achieve better feature alignment through adaptive weighting of different-scale features without extra parameters. Then, as shown in Fig. 6, we propose the Spiking Fusion Block (SF-Block) to enhance fusion by processing post-addition features. This block consists of two sub-blocks. The first has two paths, with one containing two stacked  $3 \times 3$ -LCBs and another containing a  $3 \times 3$ -LDCB (with internal depthwise convolution) followed by a  $1 \times 1$ -LCB, which enables feature extraction from different receptive fields. The second is an MS-Block for residual learning that further adjusts these features.

## V. EXPERIMENT

### A. Experimental Setup

For I-LIF neurons, the membrane time constant  $\tau$  is initialized to 0.25. The models are trained on 4 NVIDIA A6000 GPUs, using the SGD optimizer with a learning rate of 0.01. During post-processing, we use NMS, and the top 100 boxes are selected for evaluation. Additionally, we use Complete IoU (CIOU) [52] and Distribution Focal Loss (DFL) [53] for

bounding box regression, and Binary Cross Entropy (BCE) [2] for classification loss. For multiscale evaluation, following [54], we employ both original and horizontally flipped images at scale factors of 0.6, 1.0, 1.2, 1.5, and 1.8.

The COCO 2017 is a large-scale object detection benchmark with 118,287 training and 5000 validation images, which we use for training and testing, respectively. Objects from 80 categories are annotated with their classes and locations. On this dataset, we train for 400 epochs with a batch size of 64 at a resolution of  $640 \times 640$ , employing mosaic [55] and mixup [56] data augmentation for training and testing.

Following [4], [39], [54], [55], we report Average Precision (AP) as the primary metric, along with AP at IoU thresholds of 0.5 and 0.75, as well as AP for small, medium, and large objects. The firing rate, which measures neuronal activity, is another critical metric for evaluating SNNs. It is calculated as the average ratio of neuron spikes to the total number of neurons across all time steps. Additionally, we report the power consumption of the models, and the calculation method is shown in III-B.

### B. Ablation Studies

In this section, we demonstrate the effectiveness of MDSNet through backbone network comparisons and investigate how model depth, SMFM, SF-Block, and time step affect performance. For efficiency, ablation studies are conducted with 150 epochs, ensuring convergence for reliable comparison.

TABLE I  
THE ABLATION STUDY ON MDSNET. THE SPECIFIC CONFIGURATION OF THE PROPOSED MDSNET IS DETAILED IN APPENDIX B. \* AND  $\circ$  INDICATE MDSNET WITH MDS REMOVED AND REPLACED BY MEMBRANE-BASED SHORTCUTS, RESPECTIVELY.

Backbone	Depth	AP	AP <sub>50</sub>	Param (M)	Firing Rate(%)	Power (mJ)
EMS-ResNet [15]	34	43.2	59.5	22.9	14.6	28.7
SEW-ResNet [34]	34	43.2	59.7	22.9	12.2	151.9
MS-ResNet [25]	34	43.8	60.5	22.9	12.2	29.0
S-Backbone [20]	47	44.0	60.6	24.2	12.2	112.0
<b>MDSNet</b>	<b>34</b>	<b>44.8</b>	<b>61.2</b>	<b>22.0</b>	<b>11.8</b>	<b>22.9</b>
MDSNet*	34	43.7	60.5	21.9	11.4	22.1
MDSNet $\circ$	34	44.2	60.6	21.9	12.0	23.2
MDSNet	10	41.5	58.2	14.3	12.9	20.2
MDSNet	18	43.1	59.5	17.5	12.4	21.2
<b>MDSNet</b>	<b>104</b>	<b>46.5</b>	<b>63.2</b>	<b>48.2</b>	<b>9.1</b>	<b>28.8</b>

1) *The Effectiveness of MDSNet:* To demonstrate the feature extraction capabilities of MDSNet, we compare it with the most advanced SNN backbones available. For fair comparison, we construct models using the backbone networks paired with identical neck and detection head architectures. The comparison results are shown in rows 1 to 5 of Table I. These results show that MDSNet34 significantly outperforms other models in AP and AP<sub>50</sub> while achieving a lower firing rate and power consumption. Additionally, we conduct comparative experiments by replacing MDS with membrane-based shortcuts and removing MDS. As shown in rows 5 to 7 of Table I, replacing MDS with membrane-based shortcuts demonstrates the effectiveness of MDS, while removing MDS validates the importance of residual learning structures. All these modifications result in performance degradation.

TABLE II  
EFFECTIVENESS OF SMFM.

Fusion Method	Fusion Directions	AP	AP <sub>50</sub>	Param (M)	Firing Rate(%)	Power (mJ)
None	0	35.1	50.4	12.6	14.1	11.2
FPN [57]	1	38.9	56.4	14.9	14.2	15.3
PAN [58]	2	39.8	57.7	17.2	12.9	15.2
BiFPN [59]	4	38.7	56.2	12.0	14.6	12.9
<b>SMFM</b>	<b>4</b>	<b>44.8</b>	<b>61.2</b>	<b>22.0</b>	<b>11.8</b>	<b>22.9</b>
SMFM	1	41.3	58.6	21.1	13.1	25.3
SMFM	2	43.0	59.9	21.6	12.2	21.7
SMFM	6	44.2	60.7	22.1	11.3	22.1

TABLE III  
COMPARISON OF DIFFERENT FUSION BLOCKS. THE SF-BLOCK1 REFERS TO RETAINING ONLY THE FIRST SUB-BLOCK OF SF-BLOCK.

Fusion Block	AP	AP <sub>50</sub>	Param (M)	Firing Rate(%)	Power (mJ)
7×7-Conv	41.7	58.5	22.6	11.6	14.5
MS-Block	43.6	60.7	18.7	13.3	20.0
MDS-Block1	44.2	60.9	21.0	12.1	20.3
SF-Block1	43.8	60.9	20.3	12.0	20.9
<b>SF-Block</b>	<b>44.8</b>	<b>61.2</b>	<b>22.0</b>	<b>11.8</b>	<b>22.9</b>

2) *Impact of Model Depth*: In Section IV-C, we theoretically demonstrate that the MDSNet could overcome the issues of gradient vanishing or exploding, enabling the realization of deep networks. In this section, we further validate this through experiments. As shown in rows 5 and 8 to 10 of Table I, the feature extraction capability of MDSNet improves as the network depth increases. Notably, this is the first SNN backbone with over 100 layers trained on object detection datasets.

3) *The Effectiveness of SMFM*: We first compare the model without the feature fusion module with the one using SMFM. As shown in rows 1 and 5 of Table II, SMFM significantly improves AP by 9.7% with only slightly increased power consumption while also reducing firing rate. Furthermore, we compare our SMFM with the classical feature fusion modules of ANN detectors [57]–[59]. These methods are adapted for SNNs by replacing activations with I-LIF neurons. As shown in rows 2–5 of Table II, SMFM not only achieves superior performance but also effectively reduces firing rate with comparable power consumption. This demonstrates that our method effectively considers SNN characteristics and highlights the necessity of designing SNN-friendly feature fusion modules.

As shown in rows 5–8 of Table II, we compare the impact of different numbers of fusion directions on performance. To eliminate the effect of parameters, we adjust the width to maintain comparable parameters across models. Performance improves with more fusion directions when below 4, validating our analysis in IV-D. However, performance degrades beyond 4 directions, indicating that excessive complexity hinders optimization.

4) *The Effectiveness of SF-Block*: We replace the SF-Block in SMFM with other classical SNN-based blocks [25] and the simplest single convolution to demonstrate its effectiveness. As shown in Table III, SF-Block significantly outperforms other methods in both AP and firing rate, with only a slight increase

TABLE IV  
IMPACT OF DIFFERENT TIME STEPS

Model	T×D	AP	AP <sub>50</sub>	Param (M)	Firing Rate(%)	Power (mJ)
SpikeYOLO	1×2	39.9	56.3	23.1	18.8	25.7
	1×4	43.9	60.4	23.1	12.2	33.0
	1×6	45.2	61.9	23.1	9.0	36.4
SpikeDet	1×2	41.2	56.8	22.0	18.1	18.1
	1×4	44.8	61.2	22.0	11.8	22.9
	1×6	45.6	62.3	22.0	8.8	25.4

in power consumption.

5) *Impact of Time Step*: Since the SpikeDet provides more stable firing patterns and overcomes local firing saturation problems, it should theoretically achieve comparable performance with fewer time steps. To demonstrate this, we conduct corresponding experiments. Since adjusting T has been demonstrated to be inefficient in [20], we control the overall time steps of neurons by adjusting D instead. As shown in Table IV, compared to SpikeYOLO [20], our method achieves good performance even in low time steps. Moreover, performance gains remain modest as the time steps increase, demonstrating stronger robustness to variations in time steps.

#### C. Comparisons with State-of-The-Art Models

Based on the above ablation studies, we propose SpikeDet-S and SpikeDet-M using MDSNet34 and MDSNet104 as backbones, respectively. Furthermore, to explore the performance upper limit of SNN-based object detectors, we expand the width of SpikeDet-M to propose SpikeDet-L. The comparison results with state-of-the-art methods are shown in Table V. Compared to other SNN-based object detectors, our model achieves significant performance improvements (**51.4%** AP, **68.6%** AP<sub>50</sub> vs. previous 48.9% AP, 66.2% AP<sub>50</sub>, representing **+2.5%** and **+2.4%** improvements respectively) while requiring only about  $\frac{1}{2}$  of the power consumption, further strengthening the energy efficiency advantage of SNNs. Furthermore, compared to ANN-based methods, SpikeDet not only further narrows the gap between SNNs and ANNs, but also demonstrates a better trade-off between accuracy and power consumption. For example, SpikeDet-L achieves comparable accuracy to YOLOv12-M while providing **3.6** times the energy efficiency. The inference results of SpikeDet at various scales are presented in Fig. 7.

#### D. Evaluation on Object Detection Sub-Tasks

We further apply our proposed SpikeDet to two object detection sub-tasks, event camera object detection on the GEN1 dataset [27] and underwater object detection on the URPC 2019 dataset [28], and compare it with ANN and SNN baseline methods in these domains. Implementation details and dataset introductions are presented in Appendix B.

1) *Event Camera Object Detection*: As shown in Table VI, on the GEN1 dataset, our method not only significantly outperforms SNN-based object detectors but also surpasses all ANN-based methods while maintaining the energy efficiency advantage of SNNs. This marks the first time an SNN-based

TABLE V

PERFORMANCE COMPARISON WITH STATE-OF-THE-ART MODELS ON COCO 2017 VALIDATION DATASET.  $\dagger$  INDICATES RESULTS FROM MULTISCALE TESTING. THE EMS-YOLO [15] IS OUR REPRODUCED VERSION USING I-LIF NEURONS FOR FAIR COMPARISON.

Method	Model	AP	AP <sub>50</sub>	AP <sub>75</sub>	AP <sub>s</sub>	AP <sub>m</sub>	AP <sub>l</sub>	Param (M)	T×D	Firing Rate(%)	Power (mJ)
ANNs	SSD513 [60]	31.2	50.4	33.3	10.2	34.5	49.8	36.0	1	-	227.3
	ATSS [23]	39.4	57.6	42.8	23.6	42.9	50.3	32.3	1	-	377.2
	YOLOH [9]	40.3	60.9	43.5	22.9	44.4	54.0	46.0	1	-	195.5
	DETR [41]	44.9	64.7	47.7	23.7	49.5	62.3	60.6	1	-	388.3
	RetinaNet $\dagger$ [2]	41.8	62.9	45.7	25.6	45.1	54.1	56.7	1	-	759.5
	FCOS [22]	44.7	64.1	48.4	27.6	47.5	55.6	89.8	1	-	1056.8
	TOOD [61]	46.7	64.6	50.7	28.9	49.6	57.0	51.0	1	-	627.4
	CenterNet $\dagger$ [54]	47.0	64.5	50.7	28.9	49.9	58.9	191.3	1	-	1348.8
	Gold-YOLO-N [39]	39.6	55.7	-	19.7	44.1	57.0	5.6	1	-	27.6
	Gold-YOLO-S [39]	45.4	62.5	-	25.3	50.2	62.6	21.5	1	-	105.8
	Gold-YOLO-M [39]	49.8	67.0	-	32.3	55.3	66.3	41.3	1	-	197.8
	YOLOv8-N [38]	37.2	52.7	40.3	18.9	40.5	52.5	3.2	1	-	20.2
	YOLOv8-S [38]	43.9	60.8	47.6	25.3	48.7	59.5	11.2	1	-	66.2
	YOLOv8-M [38]	49.8	66.9	54.2	32.6	54.9	65.9	25.9	1	-	182.2
	RTMDet-T [55]	41.0	57.4	44.4	20.7	45.3	58.0	4.9	1	-	37.3
	RTMDet-S [55]	44.6	61.7	48.3	24.2	49.2	61.8	8.9	1	-	68.1
	RTMDet-M [55]	49.3	66.9	53.9	30.5	53.6	66.1	24.7	1	-	180.8
	YOLO-MS-XS [8]	42.8	60.0	46.7	23.1	46.8	60.1	5.1	1	-	40.0
	YOLO-MS-S [8]	45.4	62.8	49.5	25.9	49.6	62.4	8.7	1	-	69.0
	YOLO-MS [8]	49.7	67.2	54.0	32.8	53.8	65.6	23.3	1	-	178.5
	YOLOv11-N [40]	39.5	55.3	42.8	19.9	43.3	57.1	2.6	1	-	15.0
	YOLOv11-S [40]	47.0	63.9	50.6	29.9	51.6	64.4	9.4	1	-	49.5
	YOLOv11-M [40]	51.5	68.4	55.7	33.5	57.0	67.8	20.1	1	-	156.4
	YOLOv12-N [62]	40.6	56.7	43.8	20.2	45.2	58.2	2.6	1	-	15.0
	YOLOv12-S [62]	48.0	65.0	51.8	30.4	53.2	65.7	9.3	1	-	49.2
	YOLOv12-M [62]	52.5	69.6	57.1	35.9	58.2	68.8	20.2	1	-	155.3
SNNs	Spiking-YOLO [13]	25.7	-	-	-	-	-	10.2	3500	-	-
	Spike Calib [63]	25.9	-	-	-	-	-	10.2	512	-	-
	EMS-YOLO [15]	30.1	50.1	-	-	-	-	33.9	1×4	-	29.0
	M-SpikeFormer [24]	-	50.3	-	-	-	-	75.0	4	-	140.8
	SUHD [18]	-	54.6	-	-	-	-	-	4	-	-
	E-SpikeFormer [21]	-	58.8	-	-	-	-	38.7	1×8	-	119.5
	SpikeYOLO-N [20]	42.5	59.2	-	-	-	-	13.2	1×4	-	23.1
	SpikeYOLO-S [20]	45.5	62.3	49.2	25.5	50.4	61.3	23.1	1×4	12.8	34.6
	SpikeYOLO-S $\dagger$ [20]	48.0	64.8	53.4	33.1	53.2	62.0	23.1	1×4	12.8	34.6
	SpikeYOLO-M [20]	47.4	64.6	-	-	-	-	48.1	1×4	-	68.5
	SpikeYOLO-L [20]	48.9	66.2	53.4	29.3	55.0	64.2	68.8	1×4	10.4	84.2
	SpikeYOLO-L $\dagger$ [20]	51.2	68.0	56.7	36.4	56.7	65.6	68.8	1×4	10.4	84.2
	SpikeDet-S	46.2	62.6	50.5	26.8	51.2	60.8	22.0	1×4	12.3	23.8
	SpikeDet-S $\dagger$	48.2	65.3	53.6	32.4	53.2	62.2	22.0	1×4	12.3	23.8
	SpikeDet-M	48.0	64.8	52.1	27.5	54.1	63.6	48.2	1×4	9.6	30.3
	SpikeDet-M $\dagger$	50.2	67.5	55.5	34.1	55.9	64.3	48.2	1×4	9.6	30.3
	SpikeDet-L	<b>49.6</b>	<b>66.5</b>	<b>54.3</b>	<b>29.6</b>	<b>55.5</b>	<b>65.0</b>	<b>75.2</b>	<b>1×4</b>	<b>8.8</b>	<b>42.8</b>
	SpikeDet-L $\dagger$	<b>51.4</b>	<b>68.6</b>	<b>56.9</b>	<b>36.6</b>	<b>56.8</b>	<b>65.4</b>	<b>75.2</b>	<b>1×4</b>	<b>8.8</b>	<b>42.8</b>

TABLE VI

PERFORMANCE COMPARISON WITH STATE-OF-THE-ART MODELS ON GEN1 DATASET. THE  $\ddagger$  INDICATES THAT THE ACTIVATION FUNCTION OF SPIKEDET-S IS CHANGED TO RELU, CONVERTING IT TO AN ANNS VERSION.

Model	AP	AP <sub>50</sub>	Param (M)	T×D	Firing Rate(%)	Power (mJ)
RED [64]	40.0	-	24.1	-	-	>24.1
SpikeDet-S $\ddagger$	46.2	<b>66.5</b>	22.0	1	-	45.2
ASTMNet [64]	46.7	-	>100	3	-	-
RVT [65]	47.2	-	18.5	10	-	116.7
S5-Vit-B [66]	47.4	-	18.2	10	-	-
VC-DenseNet [14]	18.9	-	24.3	5	37.2	5.8
Spiking-YOLO [13]	-	45.3	7.9	5	-	0.9
EMS-YOLO [15]	31.0	59.0	14.4	5	17.8	3.4
SFOD [17]	32.1	-	11.9	5	24.4	7.3
EAS-SNN [19]	37.5	69.9	25.3	5	-	28.1
SpikingViT-B [16]	39.4	61.6	21.5	>64	18.0	-
SpikeYOLO-S [20]	38.9	66.4	23.1	5×1	-	19.7
SpikeYOLO-S	40.4	67.2	23.1	4×2	-	12.9
SpikeDet-S	<b>46.5</b>	<b>69.2</b>	<b>22.0</b>	<b>5×1</b>	<b>8.8</b>	<b>6.1</b>
SpikeDet-S	<b>47.6</b>	<b>70.1</b>	<b>22.0</b>	<b>4×2</b>	<b>13.8</b>	<b>11.5</b>

method surpasses ANNs, demonstrating that firing patterns are more crucial for SNNs in processing event data, enabling better alignment between them. Notably, our model achieves only a 1.1% AP drop when T×D is 5×1 compared to 4×2, while significantly reducing firing rate and power consumption. This demonstrates that improved firing patterns can enable SNN models to achieve excellent performance using only LIF neurons when processing event data. Furthermore, we replace I-LIF neurons with ReLU to implement an ANN version of SpikeDet on GEN1. This results in substantial performance degradation and significantly increased power consumption, highlighting the advantages of SNNs in processing event data.

2) *Underwater Object Detection*: As shown in Table VII, on the URPC 2019 dataset, SpikeDet achieves significant improvements compared to other methods in both accuracy and power consumption, reaching state-of-the-art performance among all methods. Specifically, compared to YOLOv9-S-UI, it achieves 1.4% AP improvement while reducing power

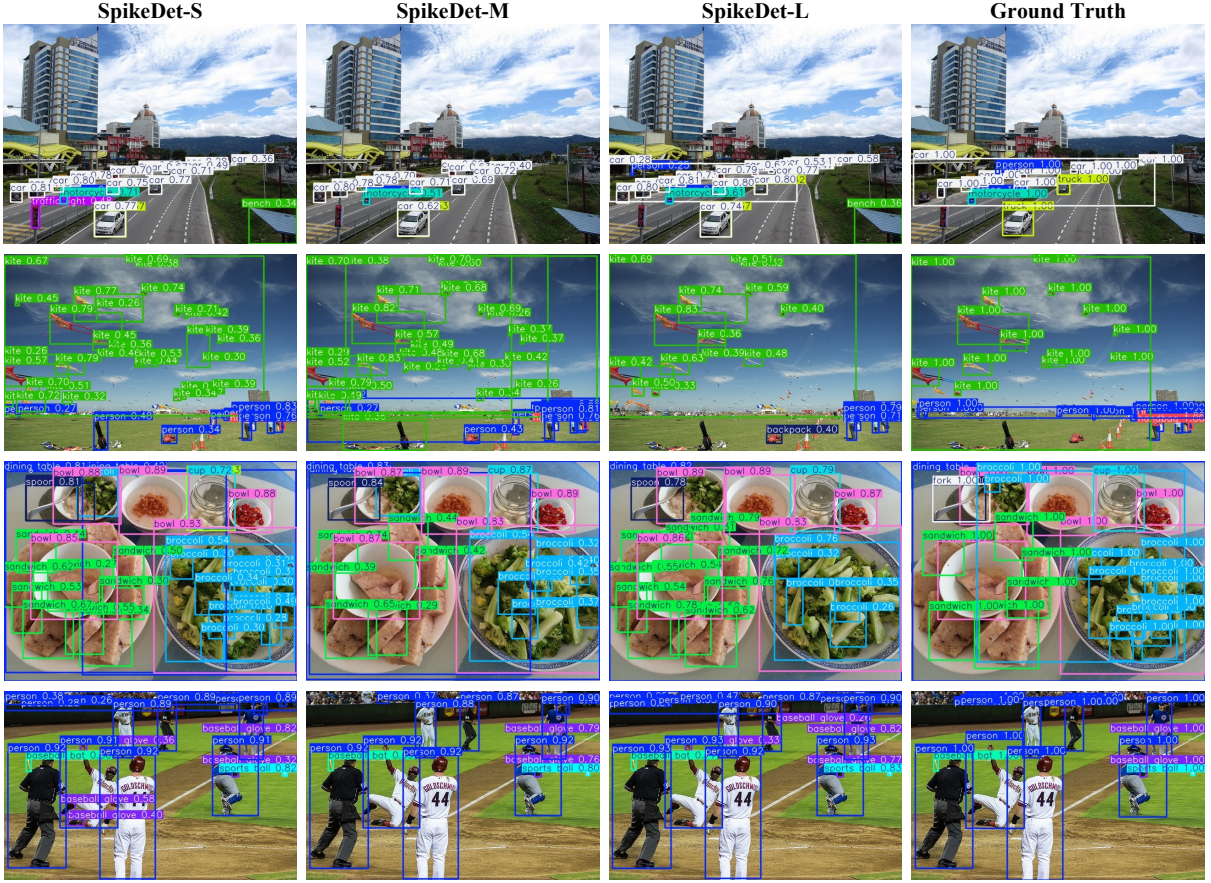


Fig. 7. Detection results on the COCO 2017 dataset. As the model scale increases, detection accuracy progressively improves.

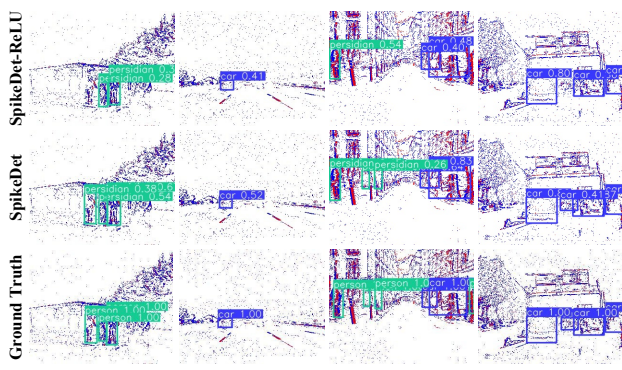


Fig. 8. Detection results on the GEN1 dataset.

consumption by 5.2 mJ.

## VI. DISCUSSION ON NEUROMORPHIC CHIP DEPLOYMENT

In the above sections, we have conducted theoretical evaluations to compare power consumption between ANNs and SNNs, following common practices in SNN research [15], [17], [19], [21], [47]. It is worth noting that the theoretical analysis excludes hardware architecture or data caching. Efficiency gains may be further amplified when SNNs are deployed on neuromorphic chips. These neuromorphic platforms,

TABLE VII  
PERFORMANCE COMPARISON WITH STATE-OF-THE-ART MODELS ON  
URPC 2019 DATASET.  $\dagger$  INDICATES RESULTS FROM MULTISCALE  
TESTING.

Model	AP	AP <sub>50</sub>	Param (M)	TxD	Firing Rate(%)	Power (mJ)
EfficientDet-D3 [59]	-	74.8	12.0	1	-	7.34
YOLOv5-S [67]	42.0	75.3	7.2	1	-	9.5
YOLOv8-N [38]	43.6	77.7	3.2	1	-	5.0
ULO [28]	-	65.1	3.8	1	-	3.0
YOLOv9-S-UI [68]	48.7	78.1	4.1	1	-	10.7
Spiking-YOLO [13]	22.4	53.7	8.7	3500	-	-
SU-YOLO [47]	42.9	78.8	7.0	4	-	3.0
SpikeYOLO-N [20]	46.9	83.1	14.2	1 $\times$ 4	12.5	5.8
SpikeYOLO-S [20]	47.9	83.8	23.1	1 $\times$ 4	12.2	8.6
<b>SpikeDet-S</b>	<b>49.2</b>	<b>84.3</b>	<b>22.0</b>	<b>1<math>\times</math>4</b>	<b>11.2</b>	<b>5.5</b>
<b>SpikeDet-S<math>\dagger</math></b>	<b>50.1</b>	<b>86.1</b>	<b>22.0</b>	<b>1<math>\times</math>4</b>	<b>11.2</b>	<b>5.5</b>

such as the Speck chip [12], operate in asynchronous mode without a global clock, leveraging spike-driven characteristics. Since I-LIF neurons are naturally suited for asynchronous operations [21], our approach can fully exploit this spike-driven paradigm. This design leads to minimal static power consumption during periods without spike inputs. Consequently, the overall energy consumption of neuromorphic computing primarily scales with the number of spike-induced ACs, further enhancing the advantages of SNNs over ANNs when static power consumption is considered.

For deployment to real hardware, we take the chip Speck as an example. First, we need to use Sinabs, a PyTorch-based deep learning library, to build and train SNN models. Through the Sinabs-Speck plugin, we can complete model quantization and configuration generation. Subsequently, we can use the Samna tool for deployment and execution.

## VII. CONCLUSION

In this paper, to overcome the local firing saturation problem and achieve better accuracy and energy efficiency, we propose SpikeDet, a novel SNN-based object detector. Specifically, the key contribution of our approach is MDSNet, which employs MDS to enhance membrane-based shortcuts with output distribution adjustment capabilities, thereby stabilizing the synaptic input distribution of neurons and achieving better neuron firing patterns in backbone features. Additionally, for the feature fusion module, we propose SMFM, which performs multiple refinement processes through a multi-directional fusion strategy, enhancing the multi-scale detection capability while preserving firing patterns. Experimental results demonstrate that our model outperforms other SNN-based models in accuracy on the COCO 2017 dataset, and even surpasses ANN-based methods on downstream tasks such as GEN1 and URPC 2019, proving its strong generalization capability. Meanwhile, it enhances SNN advantages in power consumption, achieving a superior performance-efficiency trade-off. In the future, we plan to investigate whether similar local firing saturation issues exist in other SNN-based vision tasks and propose corresponding solutions.

## REFERENCES

- C. Liu, X. Li, W. Xiao, and S. Xie, “Ccdet: Confidence-consistent learning for dense object detection,” *IEEE Trans. Image Process.*, vol. 33, pp. 2746–2758, Mar. 2024.
- T.-Y. Lin, P. Goyal, R. Girshick, K. He, and P. Dollár, “Focal loss for dense object detection,” in *Proc. IEEE/CVF Int. Conf. Comput. Vis. (ICCV)*, Oct. 2017, pp. 2980–2988.
- C. Ge, Y. Song, C. Ma, Y. Qi, and P. Luo, “Rethinking attentive object detection via neural attention learning,” *IEEE Trans. Image Process.*, vol. 33, pp. 1726–1739, Jul. 2023.
- Y. Zhao, W. Lv, S. Xu, J. Wei, G. Wang, Q. Dang, Y. Liu, and J. Chen, “Dets beat yolos on real-time object detection,” in *Proc. IEEE/CVF Conf. Comput. Vis. Pattern Recognit. (CVPR)*, Jun. 2024, pp. 16965–16974.
- Y. Liu, J. Wang, C. Huang, Y. Wu, Y. Xu, and X. Cao, “Mlfa: Toward realistic test time adaptive object detection by multi-level feature alignment,” *IEEE Trans. Image Process.*, vol. 33, pp. 5837–5848, Oct. 2024.
- L. Hu and Q. Ni, “Iot-driven automated object detection algorithm for urban surveillance systems in smart cities,” *IEEE Internet Things J.*, vol. 5, no. 2, pp. 747–754, May 2017.
- W. Lu, W. Zhang, Y. Liu, L. Xu, Y. Fan, Z. Meng, and Q. Jia, “Mfp-yolo: A multi-scale feature perception network for ct bone metastasis detection,” *Med. Biol. Eng. Comput.*, vol. 63, no. 3, pp. 629–640, Mar. 2025.
- Y. Chen, X. Yuan, J. Wang, R. Wu, X. Li, Q. Hou, and M.-M. Cheng, “Yolo-ms: Rethinking multi-scale representation learning for real-time object detection,” *IEEE Trans. Pattern Anal. Mach. Intell.*, vol. 47, no. 6, pp. 4240–4252, Feb. 2025.
- S. Wang, R. Chen, H. Wu, X. Li, and Z. Feng, “Yoloh: You only look one hourglass for real-time object detection,” *IEEE Trans. Image Process.*, vol. 33, pp. 2104–2115, Mar. 2024.
- W. Maass, “Networks of spiking neurons: The third generation of neural network models,” *Neural Netw.*, vol. 10, no. 9, pp. 1659–1671, 1997.
- N. Skatchkovsky, O. Simeone, and H. Jang, “Learning to time-decode in spiking neural networks through the information bottleneck,” in *Proc. Adv. Neural Inf. Process. Syst.*, Dec. 2021, pp. 17049–17059.
- M. Yao, O. Richter, G. Zhao, N. Qiao, Y. Xing, D. Wang, T. Hu, W. Fang, T. Demirci, and M. De Marchi, “Spike-based dynamic computing with asynchronous sensing-computing neuromorphic chip,” *Nature Commun.*, vol. 15, no. 1, 2024, Art. no. 4464.
- S. Kim, S. Park, B. Na, and S. Yoon, “Spiking-yolo: Spiking neural network for energy-efficient object detection,” in *Proc. AAAI Conf. Artif. Intell.*, vol. 34, Apr. 2020, pp. 11270–11277.
- L. Cordone, B. Miramond, and P. Thierion, “Object detection with spiking neural networks on automotive event data,” in *Proc. Int. Joint Conf. Neural Netw. (IJCNN)*, 2022, pp. 1–8.
- Q. Su, Y. Chou, Y. Hu, J. Li, S. Mei, Z. Zhang, and G. Li, “Deep directly-trained spiking neural networks for object detection,” in *Proc. IEEE/CVF Int. Conf. Comput. Vis. (ICCV)*, Oct. 2023, pp. 6555–6565.
- L. Yu, H. Chen, Z. Wang, S. Zhan, J. Shao, Q. Liu, and S. Xu, “Spikingvit: A multiscale spiking vision transformer model for event-based object detection,” *IEEE Trans. Cogn. Develop. Syst.*, vol. 17, no. 1, pp. 130–146, Jul. 2024.
- Y. Fan, W. Zhang, C. Liu, M. Li, and W. Lu, “Sfod: Spiking fusion object detector,” in *Proc. IEEE/CVF Conf. Comput. Vis. Pattern Recognit. (CVPR)*, Jun. 2024, pp. 17191–17200.
- J. Qu, Z. Gao, T. Zhang, Y. Lu, H. Tang, and H. Qiao, “Spiking neural network for ultralow-latency and high-accurate object detection,” *IEEE Trans. Neural Netw. Learn. Syst.*, vol. 36, no. 3, pp. 4934–4946, Mar. 2024.
- Z. Wang, Z. Wang, H. Li, L. Qin, R. Jiang, D. Ma, and H. Tang, “Eas-snn: End-to-end adaptive sampling and representation for event-based detection with recurrent spiking neural networks,” in *Proc. Eur. Conf. Comput. Vis. (ECCV)*, Sep. 2024, pp. 310–328.
- X. Luo, M. Yao, Y. Chou, B. Xu, and G. Li, “Integer-valued training and spike-driven inference spiking neural network for high-performance and energy-efficient object detection,” in *Proc. Eur. Conf. Comput. Vis. (ECCV)*, Sep. 2024, pp. 253–272.
- M. Yao, X. Qiu, T. Hu, J. Hu, Y. Chou, K. Tian, J. Liao, L. Leng, B. Xu, and G. Li, “Scaling spike-driven transformer with efficient spike firing approximation training,” *IEEE Trans. Pattern Anal. Mach. Intell.*, vol. 47, no. 4, pp. 2973–2990, Jan. 2025.
- Z. Tian, C. Shen, H. Chen, and T. He, “Fcos: Fully convolutional one-stage object detection,” in *Proc. IEEE/CVF Int. Conf. Comput. Vis. (ICCV)*, Oct. 2019, pp. 9627–9636.
- S. Zhang, C. Chi, Y. Yao, Z. Lei, and S. Z. Li, “Bridging the gap between anchor-based and anchor-free detection via adaptive training sample selection,” in *Proc. IEEE/CVF Conf. Comput. Vis. Pattern Recognit. (CVPR)*, Jun. 2020, pp. 9759–9768.
- M. Yao, J. Hu, T. Hu, Y. Xu, Z. Zhou, Y. Tian, B. Xu, and G. Li, “Spike-driven transformer v2: Meta spiking neural network architecture inspiring the design of next-generation neuromorphic chips,” in *Proc. Int. Conf. Learn. Represent.*, May 2024, pp. 1–23.
- Y. Hu, L. Deng, Y. Wu, M. Yao, and G. Li, “Advancing spiking neural networks toward deep residual learning,” *IEEE Trans. Neural Netw. Learn. Syst.*, vol. 36, no. 2, pp. 2353–2367, Feb. 2024.
- T.-Y. Lin, M. Maire, S. Belongie, J. Hays, P. Perona, D. Ramanan, P. Dollár, and C. L. Zitnick, “Microsoft coco: Common objects in context,” in *Proc. Eur. Conf. Comput. Vis. (ECCV)*, vol. 8693, 2014, pp. 740–755.
- P. de Tournemire, D. Nitti, E. Perot, D. Migliore, and A. Sironi, “A large scale event-based detection dataset for automotive,” 2020, arXiv:2001.08499.
- L. Wang, X. Ye, S. Wang, and P. Li, “Ulo: An underwater light-weight object detector for edge computing,” *Machines*, vol. 10, no. 8, Jul. 2022, Art. no. 629.
- J. Zhang, M. Zhang, Y. Wang, Q. Liu, B. Yin, H. Li, and X. Yang, “Spiking neural networks with adaptive membrane time constant for event-based tracking,” *IEEE Trans. Image Process.*, vol. 34, pp. 1009–1021, Jan. 2025.
- J. Tang, J.-H. Lai, X. Xie, L. Yang, and W.-S. Zheng, “Ac2as: Activation consistency coupled ann-snn framework for fast and memory-efficient snn training,” *Pattern Recognit.*, vol. 144, Dec. 2023, Art. no. 109826.
- E. O. Neftci, H. Mostafa, and F. Zenke, “Surrogate gradient learning in spiking neural networks: Bringing the power of gradient-based optimization to spiking neural networks,” *IEEE Signal Process. Mag.*, vol. 36, no. 6, pp. 51–63, Nov. 2019.
- R. Zhao, R. Xiong, J. Zhang, Z. Yu, S. Zhu, L. Ma, and T. Huang, “Spike camera image reconstruction using deep spiking neural networks,” *IEEE*

*Trans. Circuits Syst. Video Technol.*, vol. 34, no. 6, pp. 5207–5212, Oct. 2023.

[33] H. Zheng, Y. Wu, L. Deng, Y. Hu, and G. Li, “Going deeper with directly-trained larger spiking neural networks,” in *Proc. AAAI Conf. Artif. Intell.*, vol. 35, Feb. 2021, pp. 11 062–11 070.

[34] W. Fang, Z. Yu, Y. Chen, T. Huang, T. Masquelier, and Y. Tian, “Deep residual learning in spiking neural networks,” *Proc. Adv. Neural Inf. Process. Syst.*, vol. 34, pp. 21 056–21 069, Dec. 2021.

[35] P. Viola and M. Jones, “Rapid object detection using a boosted cascade of simple features,” in *Proc. IEEE/CVF Conf. Comput. Vis. Pattern Recognit. (CVPR)*, vol. 1, Dec. 2001, pp. I–I.

[36] W. Li, Z. Chen, B. Li, D. Zhang, and Y. Yuan, “Htd: Heterogeneous task decoupling for two-stage object detection,” *IEEE Trans. Image Process.*, vol. 30, pp. 9456–9469, Nov. 2021.

[37] R. Girshick, “Fast r-cnn,” in *Proc. IEEE/CVF Int. Conf. Comput. Vis. (ICCV)*, Dec. 2015, pp. 1440–1448.

[38] G. Jocher, A. Chaurasia, and J. Qiu, “Ultralytics yolov8,” 2023. [Online]. Available: <https://github.com/ultralytics/ultralytics>

[39] C. Wang, W. He, Y. Nie, J. Guo, C. Liu, Y. Wang, and K. Han, “Gold-yolo: Efficient object detector via gather-and-distribute mechanism,” *Proc. Adv. Neural Inf. Process. Syst.*, vol. 36, pp. 51 094–51 112, Dec. 2023.

[40] G. Jocher and J. Qiu, “Ultralytics yolo11,” 2024. [Online]. Available: <https://github.com/ultralytics/ultralytics>

[41] N. Carion, F. Massa, G. Synnaeve, N. Usunier, A. Kirillov, and S. Zagoruyko, “End-to-end object detection with transformers,” in *Proc. Eur. Conf. Comput. Vis. (ECCV)*, Aug. 2020, vol. 12346, pp. 213–229.

[42] W. Yu, R. Liu, D. Chen, and Q. Hu, “Explainability enhanced object detection transformer with feature disentanglement,” *IEEE Trans. Image Process.*, vol. 33, pp. 6439–6454, Nov. 2024.

[43] S. Kim, S. Park, B. Na, J. Kim, and S. Yoon, “Towards fast and accurate object detection in bio-inspired spiking neural networks through bayesian optimization,” *IEEE Access*, vol. 9, pp. 2633–2643, Nov. 2020.

[44] A. L. Hodgkin and A. F. Huxley, “A quantitative description of membrane current and its application to conduction and excitation in nerve,” *J. Physiol.*, vol. 117, no. 4, p. 500, 1952.

[45] E. M. Izhikevich, “Simple model of spiking neurons,” *IEEE Trans. Neural Netw.*, vol. 14, no. 6, pp. 1569–1572, 2003.

[46] L. F. Abbott, “Lapicque’s introduction of the integrate-and-fire model neuron (1907),” *Brain Res. Bull.*, vol. 50, no. 5–6, pp. 303–304, 1999.

[47] C. Li, W. Liu, G. Gong, X. Ding, and X. Zhong, “Su-yolo: Spiking neural network for efficient underwater object detection,” *Neurocomputing*, vol. 644, Sep. 2025, art. no. 130310.

[48] Y. Kim, H. Park, A. Moitra, A. Bhattacharjee, Y. Venkatesha, and P. Panda, “Rate coding or direct coding: Which one is better for accurate, robust, and energy-efficient spiking neural networks?” in *Proc. IEEE Int. Conf. Acoustics, Speech, Signal Process.*, May 2022, pp. 71–75.

[49] M. Taki, “Deep residual networks and weight initialization,” 2017, arXiv:1709.02956.

[50] Z. Chen, L. Deng, B. Wang, G. Li, and Y. Xie, “A comprehensive and modularized statistical framework for gradient norm equality in deep neural networks,” *IEEE Trans. Pattern Anal. Mach. Intell.*, vol. 44, no. 1, pp. 13–31, Jul. 2020.

[51] B. Poole, S. Lahiri, M. Raghu, J. Sohl-Dickstein, and S. Ganguli, “Exponential expressivity in deep neural networks through transient chaos,” *Proc. Adv. Neural Inf. Process. Syst.*, vol. 29, Dec. 2016.

[52] Z. Zheng, P. Wang, W. Liu, J. Li, R. Ye, and D. Ren, “Distance-iou loss: Faster and better learning for bounding box regression,” in *Proc. AAAI Conf. Artif. Intell.*, vol. 34, Apr. 2020, pp. 12 993–13 000.

[53] X. Li, W. Wang, L. Wu, S. Chen, X. Hu, J. Li, J. Tang, and J. Yang, “Generalized focal loss: Learning qualified and distributed bounding boxes for dense object detection,” in *Proc. Adv. Neural Inf. Process. Syst.*, vol. 33, Dec. 2020, pp. 21 002–21 012.

[54] K. Duan, S. Bai, L. Xie, H. Qi, Q. Huang, and Q. Tian, “Centernet++ for object detection,” *IEEE Trans. Pattern Anal. Mach. Intell.*, vol. 46, no. 5, pp. 3509–3521, Dec. 2023.

[55] C. Lyu, W. Zhang, H. Huang, Y. Zhou, Y. Wang, Y. Liu, S. Zhang, and K. Chen, “Rtmdet: An empirical study of designing real-time object detectors,” 2022, arXiv:2212.07784.

[56] H. Zhang, M. Cisse, Y. N. Dauphin, and D. Lopez-Paz, “Mixup: Beyond empirical risk minimization,” 2018, arXiv:1710.09412.

[57] T.-Y. Lin, P. Dollár, R. Girshick, K. He, B. Hariharan, and S. Belongie, “Feature pyramid networks for object detection,” in *Proc. IEEE/CVF Conf. Comput. Vis. Pattern Recognit. (CVPR)*, Jul. 2017, pp. 2117–2125.

[58] S. Liu, L. Qi, H. Qin, J. Shi, and J. Jia, “Path aggregation network for instance segmentation,” in *Proc. IEEE/CVF Conf. Comput. Vis. Pattern Recognit. (CVPR)*, Jun. 2018, pp. 8759–8768.

[59] M. Tan, R. Pang, and Q. V. Le, “Efficientdet: Scalable and efficient object detection,” in *Proc. IEEE/CVF Conf. Comput. Vis. Pattern Recognit. (CVPR)*, Jun. 2020, pp. 10 781–10 790.

[60] W. Liu, D. Anguelov, D. Erhan, C. Szegedy, S. Reed, C.-Y. Fu, and A. C. Berg, “Ssd: Single shot multibox detector,” in *Proc. Eur. Conf. Comput. Vis. (ECCV)*, Oct. 2016, vol. 9905, pp. 21–37.

[61] C. Feng, Y. Zhong, Y. Gao, M. R. Scott, and W. Huang, “Tood: Task-aligned one-stage object detection,” in *Proc. IEEE/CVF Int. Conf. Comput. Vis. (ICCV)*, Oct. 2021, pp. 3490–3499.

[62] Y. Tian, Q. Ye, and D. Doermann, “Yolov12: Attention-centric real-time object detectors,” 2025, arXiv:2502.12524.

[63] Y. Li, X. He, Y. Dong, Q. Kong, and Y. Zeng, “Spike calibration: Fast and accurate conversion of spiking neural network for object detection and segmentation,” 2022, arXiv:2207.02702.

[64] E. Perot, P. De Tournemire, D. Nitti, J. Masci, and A. Sironi, “Learning to detect objects with a 1 megapixel event camera,” *Proc. Adv. Neural Inf. Process. Syst.*, vol. 33, pp. 16 639–16 652, Dec. 2020.

[65] M. Gehrig and D. Scaramuzza, “Recurrent vision transformers for object detection with event cameras,” in *Proc. IEEE/CVF Conf. Comput. Vis. Pattern Recognit. (CVPR)*, Jun. 2023, pp. 13 884–13 893.

[66] N. Zubic, M. Gehrig, and D. Scaramuzza, “State space models for event cameras,” in *Proc. IEEE/CVF Conf. Comput. Vis. Pattern Recognit. (CVPR)*, Jun. 2024, pp. 5819–5828.

[67] G. Jocher, “Ultralytics yolov5,” 2020. [Online]. Available: <https://github.com/ultralytics/yolov5>

[68] W. Pan, J. Chen, B. Lv, and L. Peng, “Optimization and application of improved yolov9s-ui for underwater object detection,” *Appl. Sci.*, vol. 14, no. 16, Aug. 2024, Art. no. 7162.

## APPENDIX A PROOF OF THE PROPOSITIONS

### A. Proof of Proposition 2

**Proposition 2.** *For I-LIF neurons, if the input follows  $\mathbf{x}^{t,n-1} \sim \mathcal{N}(0, \sigma_{in}^2)$ , then the membrane potential follows  $\mathbf{u}^{t,n} \sim \mathcal{N}(0, \sigma_{out}^2)$ , where  $\sigma_{out}^2$  is proportional to  $\sigma_{in}^2$ .*

From Eqs. 1 and 3 in the main paper, we obtain:

$$\begin{aligned} \mathbf{u}^{t,n} &= \tau(\mathbf{u}^{t-1,n} - \mathbf{o}^{t-1,n}) + \mathbf{x}^{t,n-1} \\ &= \tau[\tau(\mathbf{u}^{t-2,n} - \mathbf{o}^{t-2,n}) - \mathbf{o}^{t-1,n}] + \mathbf{x}^{t,n-1} \\ &= \tau^{t-1} \mathbf{x}^{1,n-1} - \sum_{p=1}^{t-1} \tau^p \mathbf{o}^{t-p,n} + \sum_{p=1}^t \tau^p \mathbf{x}^{t-p,n-1}. \end{aligned} \quad (15)$$

Since  $\tau$  is a tiny constant, which is only 0.25 in our implementation, the above equation can be simplified to:

$$\mathbf{u}^{t,n} = \mathbf{x}^{t,n-1} + \tau \mathbf{x}^{t-1,n-1} - \tau \mathbf{o}^{t-1,n}. \quad (16)$$

Moreover, since I-LIF can fire integer-valued spikes, each spike emission reduces the membrane potential to a level close to 0. Therefore, we can assume that the last spike is fired at time step  $t'$ , and thus ignore the influence of  $\mathbf{o}$  on the membrane potential, yielding:

$$\mathbf{u}^{t,n} = \mathbf{x}^{t,n-1} + \tau \mathbf{x}^{t-1,n-1}. \quad (17)$$

Because we employ tdBN for normalization,  $\mathbf{x}$  is independently and identically distributed for each time step  $t$ . Thus, we can conclude that  $\mathbf{u}^{t,n} \sim \mathcal{N}(0, \sigma_{out}^2)$ , where  $\sigma_{out}^2$  is proportional to  $\sigma_{in}^2$ .

### B. Proof of Proposition 3

**Proposition 3.** *For MDSNet, when the encoding layer output follows  $\mathbf{x}^t \sim \mathcal{N}(0, 1)$  and each block output follows  $\mathbf{x}^{t,j} \sim \mathcal{N}(0, 1)$ , the network satisfies:  $\phi(\mathbf{J}\mathbf{J}^T) \approx 1$ .*

TABLE VIII

**THE STRUCTURE OF MDSNET FOR COCO 2017.** THE OUTPUT SIZE COLUMN SPECIFIES THE SPATIAL RESOLUTION AND CHANNEL COUNT OF FEATURE MAPS PRODUCED AT EACH STAGE. THE NUMBERS IN PARENTHESES INDICATE THE NUMBER OF MS-BLOCKS CONTAINED IN THE RESIDUAL PATH OF THE MDS-BLOCK.

Stage	Output Size	MDSNet10	MDSNet18	MDSNet34	MDSNet104
Encoding	320×320, 64	Encoding Block			
Conv1	160×160, 64	MS2Block2(0)	MS2Block2(1)	MS2Block2(2)	MS2Block2(2)
Conv2	80×80, 128	MS2Block2(0)	MS2Block2(1)	MS2Block2(1) MS2Block1(1)	MS2Block2(3) MS2Block1(3)
Conv2	40×40, 256	MS2Block2(0)	MS2Block2(1)	MS2Block2(2) MS2Block1(2)	MS2Block2(15) MS2Block1(15)
Conv4	20×20, 512	MS2Block2(0)	MS2Block2(1)	MS2Block2(2)	MS2Block2(3) MS2Block1(3)
Conv5	20×20, 512	SpikeSPPF			

**Theorem 2. (Theorem 4.2. in [50])** Given  $\mathbf{J} := \sum_j \mathbf{J}_j$ , where  $\mathbf{J}_j$  is a series of independent random matrices. If at most one matrix in  $\mathbf{J}_j$  is not a central matrix, we have

$$\phi\left(\mathbf{J}\mathbf{J}^T\right) = \sum_j \phi\left(\mathbf{J}_j\mathbf{J}_j^T\right). \quad (18)$$

We first analyze each MDS-Block, which consists of two distinct pathways: the residual path and the shortcut path. Consequently, we designate their respective Jacobian matrices as  $\mathbf{J}_{\text{res}}$  and  $\mathbf{J}_{\text{sc}}$ .

For the residual path, since all its components satisfy Definition 2 for MDS-Block1 and MDS-Block2 [15], [33], [50], we can derive:

$$\alpha_2^{l,\text{res}} = \phi(\mathbf{J}_{\text{res}}\mathbf{J}_{\text{res}}^T)\alpha_2^{l-1}, \quad (19)$$

$$\phi(\mathbf{J}_{\text{res}}\mathbf{J}_{\text{res}}^T) = \frac{\alpha_2^{l,\text{res}}}{\alpha_2^{l-1}}. \quad (20)$$

The same applies to the shortcut path, therefore:

$$\phi(\mathbf{J}_{\text{sc}}\mathbf{J}_{\text{sc}}^T) = \frac{\alpha_2^{l,\text{sc}}}{\alpha_2^{l-1}}. \quad (21)$$

Based on Theorem 2, we can derive for MDS-Block1 and MDS-Block2:

$$\phi(\mathbf{J}_{\text{MDS-Block}}\mathbf{J}_{\text{MDS-Block}}^T) = \frac{\alpha_2^{l,\text{res}} + \alpha_2^{l,\text{sc}}}{\alpha_2^{l-1}}. \quad (22)$$

Therefore, if the encoding layer output follows  $\mathbf{x}^t \sim \mathcal{N}(0, 1)$  and each block output follows  $\mathbf{x}^{t,j} \sim \mathcal{N}(0, 1)$ , we can derive:

$$\phi(\mathbf{J}_{\text{MDS-Block}}\mathbf{J}_{\text{MDS-Block}}^T) = 1. \quad (23)$$

Thus, for the entire MDSNet, according to the above equation and the derivation from Theorem 1, we can derive:

$$\phi(\mathbf{J}\mathbf{J}^T) \approx 1. \quad (24)$$

## APPENDIX B MORE EXPERIMENTAL SETUP

*1) Datasets Introduction:* The GEN1 dataset [27] represents the initial large-scale collection for object detection using event cameras. It comprises car footage spanning over 39 hours, captured by the GEN1 device with a spatial resolution of 304×240. The dataset includes bounding box annotations for vehicles and pedestrians, provided at rates of 1 to 4Hz. These labels accumulate to a total exceeding 255,000 across the recordings.

The URPC 2019 dataset [28] is designed for the 2019 Underwater Robot Picking Contest and comprises 4,707 annotated underwater images across four marine object categories: scallops, starfish, echinus, and holothurian. The dataset splits include 3,767 training images, 695 validation images, and 245 test images.

*2) More Implementation Details:* The MDSNet structure is detailed in Table VIII. For SpikeDet-L, we increase the channel dimensions of MDSNet104 by a factor of 1.25 to improve model performance. On the Gen1 dataset, we employ the zoom-in and zoom-out augmentation strategies from [65]. The model is trained for 100 epochs with a batch size of 64. On the URPC 2019 dataset, we use mosaic augmentation and, similar to [28], [47], [68], resize images to 320×320 and train for 300 epochs with a batch size of 64.

## APPENDIX C MORE VISUALIZATION

In this section, we present the visualization results of our model on the URPC 2019 dataset, as shown in Fig. 9. These results demonstrate that our model can achieve excellent performance on the object detection sub-tasks.

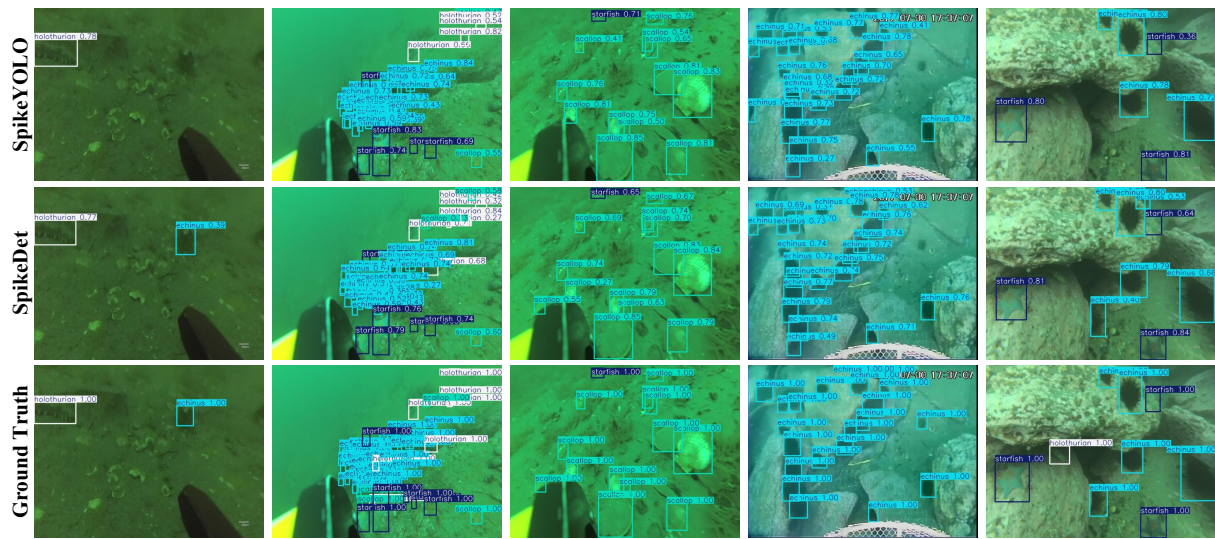


Fig. 9. Detection result on the URPC 2019 dataset.